41st AIAA/ASME/SAE/ASEE Joint Propulsion Conference
Tucson, AZ, July 10-13, 2005

AIAA-2005-3690

Plasma Processes of DC Ion Thruster Discharge Chambers

Richard Wirz, Ira Katz
Jet Propulsion Laboratory, California Institute of Technology, Pasadena, CA

This study has advanced state-of-the-art discharge modeling and revealed important aspects of discharge plasma processes. These extensions of existing ion thruster technology and understanding are necessary to fulfill the needs of future space missions. A multi-component hybrid 2-D computational Discharge Chamber Model (DCM) was developed to help identify important ion thruster discharge processes and investigate miniaturization issues. The model is designed to integrate thruster component (cathode and grid) wear models to allow the determination of thruster life and long-term performance. The model accounts for the five major chamber design parameters (chamber geometry, magnetic field, discharge cathode, propellant feed, ion extraction grid characteristics) and self-consistently tracks the effects of the four plasma species (neutral propellant atoms, secondary electrons, primary electrons, and ions). Results from the model show good agreement with experimental data at two operating points for the 30cm NSTAR ion thruster. A thruster design sensitivity performed with DCM suggests that NSTAR thruster performance is greatly enhanced by increasing the strength of the middle magnet ring. The model analyses show that the peak observed in the NSTAR beam profile is due to double ions that are created by over-confinement of primary electrons on the thruster axis. Design sensitivity results show that, at the NSTAR thruster scale, efficient *confinement* of primary electrons is relatively easy to achieve; therefore, efforts to improve thruster performance should focus on effectively *utilizing* the primary electrons to minimize double ion production and maximize the number of single ions extracted to the beam. DCM results also show that non-classical effects are important for predicting the perpendicular mobility of secondary electrons in ion thruster discharges. Good agreement with experimental data was found by weighting the influence of Bohm-type diffusion by considering the non-uniform levels of ionization in the discharge. It was found that ion thrusters operate in an intermediately ionized plasma regime that is between fully and weakly ionized approximations. The observations from this study have furthered the understanding of discharge processes and should improve future ion thruster design and modeling efforts. DCM advances state-of-the-art ion thruster modeling and provides a framework for a complete thruster model that can be used for long-life performance assessment and life validation.

Nomenclature

A = area

$\mathbf{B}$ = magnetic flux density

$\underline{\underline{\mathbf{D}}}$ = plasma diffusion tensor

$D_{||}$ = parallel plasma diffusion coefficient

$D_{\perp}$ = parallel plasma diffusion coefficient

$\mathbf{E}$ = electric field

e = electron charge

f_{inel} = secondary inelastic collision fraction

f_A = fraction of ion current to anode surfaces

f_B = fraction of ion current to the beam

f_C = fraction of ion current to cathode surfaces

F_B = beam flatness

F_T = thrust correction due to divergence of beam

$\hat{h}$ = unit direction vector

I_{sp} = specific impulse

j = current density

j_B^+ = beam current density due to singly charged ions

j_B^{++} = beam current density due to doubly charged ions

j_{screen}^+ = screen current density due to singly charged ions

©2004 by the American Institute of Aeronautics and Astronautics, Inc. The U.S. Government has a royalty-free license to exercise all rights under the copyright claimed herein for Governmental purposes. All other rights are reserved by the copyright owner.

j_{screen}^{++} = screen current density due to doubly charged ions

J_B = total beam current

J_B^+ = beam current due to singly charged ions

J_B^{++} = beam current due to doubly charged ions

J_D = discharge current

J_{DCH} = discharge cathode heater current

J_p = primary electron current

J_{screen} = screen grid ion current

k = Boltzmann's constant

K = collision rate constant

K_{iz}^p = ionization collision rate constant due to primary electrons

K_{iz}^s = ionization collision rate constant due to secondary electrons

K_{ex}^s = excitation collision rate constant due to secondary electrons

K_{el}^s = elastic collision rate constant due to secondary electrons

K_{iz}^o = total ionization collision rate constant of neutral atoms

K_{ex}^o = excitation collision rate constant of neutral atoms

K_{iz}^+ = double ionization collision rate constant of single ions

K_{slow}^s = effective primary electron slowing rate constant due to secondary electrons

m = mass

m_e = electron mass

m_i = ion mass

$\dot{m}_d$ = discharge chamber propellant mass flow rate

$\dot{m}_{loss}$ = mass flow rate of propellant loss

$\underline{\underline{\mathbf{M}}}_e$ = electron mobility tensor

$\underline{\underline{\mathbf{M}}}_i$ = ion mobility tensor

$M_E^{\perp}$ = electric field perpendicular mobility

n_i = ion number density

n_+ = single ion number density

n_{++} = double ion number density

n_o = neutral atom number density

n_p = primary electron number density

n_s = secondary electron number density

$\dot{n}_i$ = total ion generation rate density

$\dot{n}_{++}$ = double ion generation rate density

$\dot{n}_i^p$ = ion generation rate density due to primary electrons

$\dot{n}_i^s$ = ion generation rate density due to secondary electrons

$\dot{n}_s$ = secondary generation rate density

$\dot{n}_{ex}^p$ = collision rate density for primary excitation of neutral ions

$\dot{n}_{slow}^p$ = collision rate density for primary slowing by secondary electrons

$\dot{n}_i^p$ = ion generation rate density due to primary electrons

$\mathbf{P}$ = pressure

P_E = total thruster input power

P_o = miscellaneous thruster input power

P_T = thrust (jet) power

P_{iz} = probability of ionization collision

P_{ex} = probability of excitation collision

P_{slow} = probability of slowing collision

(P_{ps}, P_{pw}, P_{piz}, P_{ps}, P_{sw}, P_{siz}, P_{sx}) = electron power loss mechanisms (Described in text)

q = electric charge

r = distance from thruster axis

r_{ce} = electron cyclotron radius

$\mathbf{R}_i$ = ion momentum transfer due to collisions

$\mathbf{R}_e$ = electron momentum transfer due to collisions

t = time

T_e = electron temperature

T_i = ion temperature

T_p = primary electron temperature

T_s = secondary electron temperature

T_s^{inel} = effective secondary electron temperature for inelastic collisions

T_o = neutral atom temperature

T_{ideal} = ideal thrust

T_{corr} = corrected thrust

u_{Bohm} = Bohm velocity

u_+^{Bohm} = Bohm velocity for single ions

$\mathbf{u}$ = drift velocity

$\mathbf{u}_e$ = electron drift velocity

$\mathbf{u}_i$ = ion drift velocity

V = view factor

V_{accel} = accelerator grid voltage

V_B = beam voltage

V_c = cathode operation voltage

V_{cell} = computational cell volume

V_D = discharge voltage

V_{DPP} = distributor pole piece voltage

V_{Fil} = filament voltage drop

V_p = primary electron voltage

w = particle velocity

y = neutral flux

Y = neutral flow rate

z = axial distance

Greek Symbols

α = double ion thrust correction

β = neutral ionization fraction (Neutral Atom Sub-Model)

γ_{nc} = non-classical collision parameter

Γ = particle flux

Γ_e = electron flux

δ_D = plasma magnetization

δ_ν = electron collision ratio

ε_B = discharge loss

$\langle \varepsilon \rangle$ = average energy

ε_{iz} = ionization energy

κ = thermal diffusion coefficient

λ = mean free path

$\ln\Lambda$ = Coulomb logarithm

μ = mobility coefficients (defined in Appendix G)

μ^* = simplified mobility coefficients (Section 4.6)

ν = collision frequency

ν_{ie} = ion-electron collision frequency

ν_{ei} = electron-ion collision frequency

ν_{io} = ion-neutral collision frequency

ν_{eo} = electron-neutral collision frequency

ν_{CEX} = charge-exchange collision frequency

ν_{ei} = electron-ion collision frequency

$\nu_{e\text{-}o}$ = neutral-centered electron collision frequency

$\nu_{e\text{-}i}$ = ion-centered electron collision frequency

$\nu_{i\text{-}o}$ = neutral-centered ion collision frequency

$\nu_{e\text{-}gen}$ = effective collision frequency due to electron generation rate

$\nu_{i\text{-}gen}$ = effective collision frequency due to ion generation rate

σ = collision cross-section

ϕ = electric potential

ψ = effective potential

Ψ = configuration factor

ω_{ce} = electron cyclotron frequency

Ω_e = electron Hall parameter

η_E = electrical efficiency

η_T = total efficiency

η_{ud} = discharge propellant utilization efficiency

$\eta_{ud\,[Gas]}$ = discharge propellant utilization efficiency per Neutral Atom Sub-Model

$\eta_{ud\,[Beam]}$ = discharge propellant utilization efficiency per Ion Diffusion Sub-Model

$\eta_{ud\,[*]}$ = discharge propellant utilization efficiency (not corrected for double ions)

ζ_o = grid transparency to neutral atoms

ζ_i = grid transparency to ions

I. Units:

This study uses mks units of the International System (SI) with the exception that energies are frequently given in terms of electron volts (eV).

sccm ≡ Standard Cubic Centimeters per Minute. <u>For xenon: 1 sccm ≈ 0.09839 mg/s at STP</u>.

eV/ion ≡ (Watts of Discharge Power)/(Amp of Beam Current) for discharge loss, ε_B

I. Introduction

A. Background and Motivation

Ion thrusters are highly efficient electrostatic ion accelerators used for in-space propulsion. Past experimental and analytical efforts have resulted in thruster designs that exhibit attractive performance; however, many of the processes involved with the discharge plasma are still not well understood. A better understanding of these processes is necessary to advance the state of the art of ion thruster design and performance. The validation of high-power, long-life ion thrusters for the missions in Section 1.2 requires a better understanding of ion thruster performance, life, and scaling. Experimental life tests, such as the 8,200-hour and 30,000-hour NSTAR life test, are impractical and prohibitively expensive for validating ion thruster life and performance for future long-duration, high-power missions [7,5]. Thruster component wear changes the performance of the thruster over the life of the mission. As discussed in Section 2.4, existing ion thruster discharge theory and models are insufficient to provide necessary inputs to multi-dimensional computational models that are designed to predict the wear rates and long-life performance behavior of thruster components (i.e., discharge cathode and grids) [8,9]. Therefore, a multi-dimensional discharge model that can be used with cathode and grid wear models is important to validating the long-

term performance and life of future ion thrusters. Such a model can also be used to aid design efforts to increase propellant efficiency, which would yield significant propellant mass savings for large propellant throughput missions. This study presents a multi-dimensional computational model of an ion thruster discharge that self-consistently accounts for the behavior and interactions of the discharge plasma species for a large range of thruster geometries and magnetic fields. This Discharge Model is designed to help identify important discharge plasma processes, aid in the design of ion thrusters, and integrate thruster component and wear models.

To date, multi-dimensional modeling of ion thruster discharges has been almost entirely limited to predicting two important parameters in Brophy's zero-dimensional model: the primary utilization factor, C_o, which is proportional to the average distance a primary would travel in the absence of inelastic collisions, and, f_B, the fraction of discharge ions extracted to the beam. Previous discharge modeling efforts have provided useful information to the performance of conventional ion thruster designs; however, these models have not been used to successfully guide ion thruster design and optimization. These models are also insufficient to aid in the prediction of long-term performance since they do not provide sufficient information for cathode and grid wear models [9,8]. The model presented herein is being designed to handle non-uniform plasma densities and non-uniform neutral atom temperatures and densities. This additional resolution over existing models that allow the model to predict important discharge chamber performance issues such as non-uniform neutral loss through the ion extraction grids and to address the complicated behavior in the discharge cathode plume. Recent efforts in the design of both large ion thruster, such as NEXIS [ref#7jpc04], and small ion thrusters, such as the Miniature Xenon Ion (MiXI) thruster [ref#8jpc04], will benefit greatly from an accurate discharge model.

B. Objective

The objective of this investigation is to create an electron bombardment ion thruster discharge chamber model to accurately predict the plasma behavior within the thruster. This model is intended to provide the framework for a full ion thruster model that can be self-consistently integrated with existing and ongoing cathode and grid wear and performance models[9-12]. The accuracy of the model is validated be comparing the results to NSTAR data. The model is also used to predict the performance of alternative thruster configurations. The model provides sufficient resolution to investigate basic characteristics of DC ring-cusp ion thruster discharges, such as:

1) What is the relative importance of the primary and secondary electron species?
2) Why do some thrusters have poor beam profiles (low beam flatness)? If the profile possesses a double ion peak, what mechanisms are causing the double ions?
3) What is the diffusive behavior of the discharge plasma? Does it behave as weakly or fully ionized plasma?
4) To what degree is the discharge plasma magnetized?

II. General Approach

The multi-component hybrid 2-D computational Discharge Chamber Model (DCM) has been developed to simulate ion thruster discharge processes and provide a framework for a full thruster model. The model is designed to integrate thruster component (cathode and grid) wear models to allow the determination of thruster life and long-term performance. Figure figD1 gives an overview of the major components of DCM and its relationship with the cathode and ion optics models. The model accounts for the five major chamber design parameters (chamber geometry, magnetic field, discharge cathode, propellant feed, ion extraction grid characteristics) and self-consistently tracks the effects of the four plasma species (neutral propellant atoms, secondary electrons, primary electrons, and ions). As discussed below, the model initially assumes a low density thermal plasma and then uses mixing and relaxation parameters to incrementally reach a final steady-state solution.

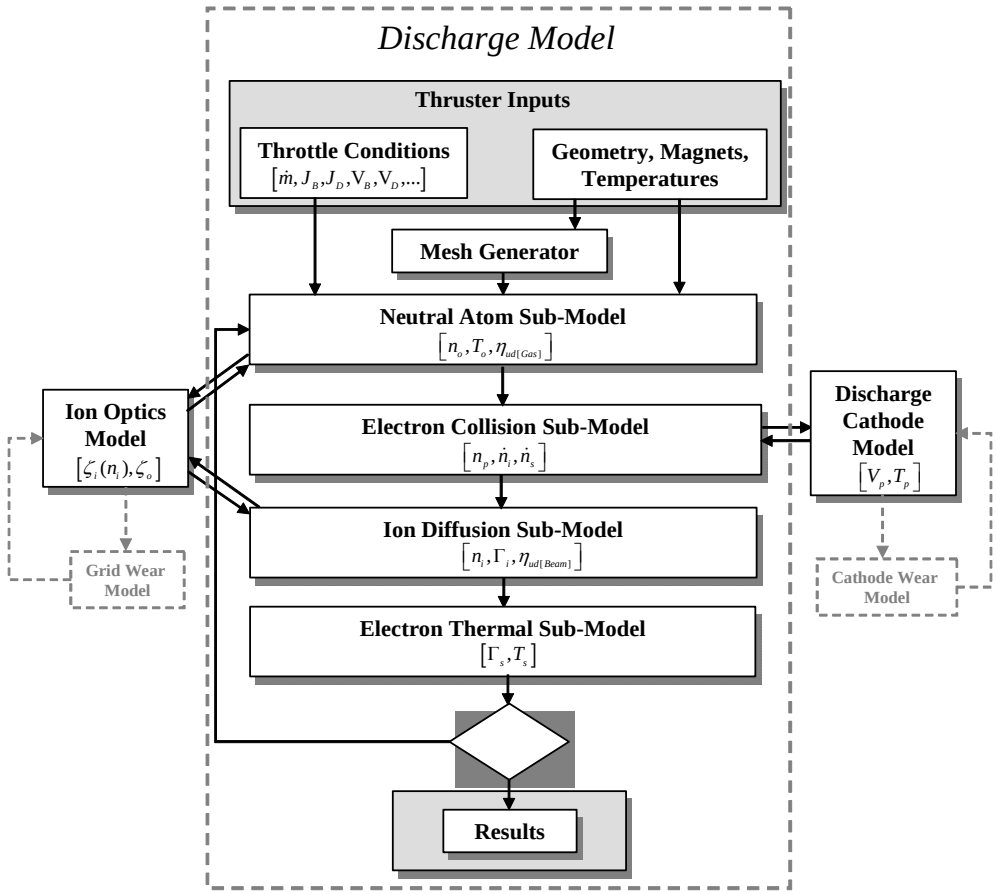

Figure 4.1-1. Discharge Model Overview

III. Model Components

A. Thruster Inputs

The model can accommodate a wide range of axisymmetric thruster geometries that can be simply defined in the model input as a 2-D contour of the discharge surface. The operating conditions used for the model include basic thruster inputs such as propellant flow rate and feed locations, thruster voltages, and cathode current. To simulate a certain operating condition, the model uses basic thruster inputs, i.e.:

1) J_D - discharge current
2) V_B, V_D, V_{accel} – beam, discharge, and accel grid voltage
3) $\dot{m}_d$ - discharge propellant flow rates
4) Thruster geometry
5) Magnet properties and location
6) Ion optics geometry (to determine $\zeta_i(n_i)$, ζ_o)
7) Surface temperatures

The magnetic rings for ion thrusters are typically composed of many rectangular magnets. The field due to the individual permanent magnets is approximated by discrete magnetic dipole moments whose orientation and strength are determined by entering the magnet properties, sizes, number per ring, 2-D location of the ring, magnet orientation, and temperature. With this information the magnetic flux density vectors, B (Tesla), and the magnetic vector potential, A (Tesla·meters), are determined at any point by summing the

effects of all magnets. The magnetic field for each magnet is found using a simple dipole approximation with a near magnet correction as described in references [refthesis] and [refJPC05].

B. Computational Meshes

DCM simulates thruster surfaces made up of axisymmetric geometric shapes such as cylinders, cones, planes, and spheres. This allows the model to simulate almost any axisymmetric discharge shape of interest. In the model, these surfaces are simply defined in the model input as a contour of the discharge surface as shown in Figure 4.1-2. Each element of the Boundary Mesh is assigned a voltage (cathode or anode), temperature, and transparency. The ion extraction grid transparency to ions and neutrals is a function of the local densities as described in Section 4.4. On-axis propellant feeds, such as hollow cathodes, are considered point sources while off-axis feeds are assumed to be uniformly distributed plenums.

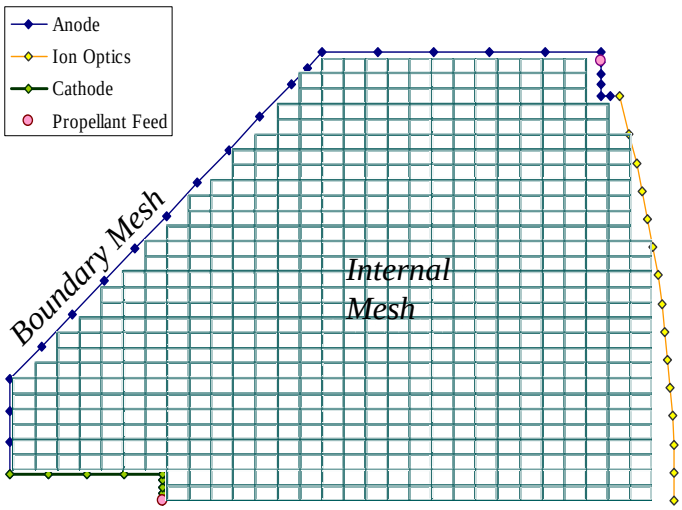

Figure 4.1-2. Internal Mesh and surrounding Boundary Mesh with surface type definitions and propellant feed locations

The Boundary Mesh is used in all sub-models as a precise representation of the internal surfaces of the thruster. The volume of the discharge is defined by a 2-D Internal Mesh that is used to track the plasma properties determined in each sub-model. Figure 4.1-2 shows an example of an Internal Mesh and Boundary Mesh for the NSTAR geometry. For this example the meshes are not entirely commensurate due mainly to the curved grids and the conical surface; however, simple blending methods are used to communicate between the meshes and conserve appropriate quantities. The Internal mesh is composed only of elements fully contained within the discharge chamber. It is not completely necessary for this mesh to fully resolve the chamber boundary since the precise shape of the boundary is fully resolved by the Boundary Mesh. It was found that the model results did not change noticeably with increased mesh resolution beyond that shown in Figure 4.1-2. References REFJPC04 and RefThesis discuss the advantages and complexities of using a magnetically aligned computational for Internal Mesh in future versions of this model; however, the orthogonal mesh is sufficient for the discharge processes examined herein.

Convergence and Mixing Techniques

The model reaches a steady-state solution by first assuming very low density thermal plasma (at least an order of magnitude less than the anticipated final condition) and incrementally increasing the primary electron current until full primary current is reached. Mixing parameters are used to avoid overly large gradients for the self-consistent solution of an iteration. Key parameters, such as ionization rates, ion density, and primary density are mixed at the beginning of an iteration of the model using relaxation parameters. Model convergence is tracked by determining relative values of “gas” and “beam” discharge propellant efficiencies, given by

$$\eta_{ud[Gas]} = \frac{\dot{m}_d - \dot{m}_{loss}}{\dot{m}_d} \qquad [4.1\text{-}1]$$

$$\eta_{ud[Beam]} = \frac{\left(J_B^{+} + J_B^{++}/2\right) m_i}{e\dot{m}_d} \qquad [4.1\text{-}2]$$

where J_B^+ and J_B^{++} are the beam currents due to single and double ions, respectively; $\dot{m}_d$ is the total propellant flow rate into the discharge chamber. Equation 4.1-1 is the propellant efficiency that is calculated by the Neutral Atom Sub-Model by tracking the loss of unused propellant, $\dot{m}_{loss}$. Equation 4.1-2 is the propellant efficiency from the Ion Diffusion Sub-Model that calculates the rate at which ions (of all charges) are extracted into the beam. The equality of propellant efficiency per equations 4.1-1 and 4.1-2 implies conservation of propellant such that $\dot{m}_d = \dot{m}_{loss} + \left(J_B^+ + J_B^{++}/2\right) m_i / e$. When conservation of propellant ($\eta_{ud\ [Gas]} \sim \eta_{ud\ [Beam]}$) persists for several iterations, it is found that all other parameters determined by DCM (e.g., densities, temperatures) are very near their steady-state solution. Many experimental results calculate propellant efficiency by assuming that the beam is entirely composed of single ions, resulting in the expression

$$\eta_{ud[*]} = \frac{\left(J_B^+ + J_B^{++}\right) m_i}{e\dot{m}_{prop}} \qquad [4.1\text{-}3]$$

Using Equation 4.1-3, the model calculates propellant efficiency values to compare with experimental data.

Discharge Plasma Parameter Ranges

One of the main difficulties associated with modeling an ion thruster discharge is the wide range of plasma parameters throughout the full extent of the domain. Table 4.1-1 gives approximate plasma conditions on-axis (r=0), in the bulk of the plasma (r=R/2), and near the anode (r=R), for the NSTAR (R=30cm) thruster. These approximate conditions were determined from experimental measurements and early computational evaluations. The mean free paths, cyclotron radii, and Hall parameters for these conditions are given in Table 4.1-2 (see Reference [50] and [refThesis] for formulations). The results from this table are used in the following sections to guide to formulation of the various sub-models.

Table 4.1-1. Approximate NSTAR Plasma Conditions

	n [m^{-3}]	n_o [m^{-3}]	T_s [eV]	E_p [eV]	T_o [eV]	|B| [G]
NSTAR (TH15)						
r=0	1E+17	5E+18	3.5	20	0.04	25
r=R/2	2.5E+17	2.5E+18	4	20	0.06	30
r=R	5E+17	8E+17	4.5	20	0.11	100

Table 4.1-2. Approximate NSTAR Plasma Parameters

	λ_n [cm]	λ_p [cm]	$\lambda_{p\text{-}n}$ [cm]	λ_{slow} [cm]	λ_i [cm]	r_{ci} [cm]	r_{ce} [cm]	Ω_i	Ω_e
NSTAR (TH15)									
r=0	37.15	59.2	62.0	1327.7	2.166	44.2	0.285	0.05	601
r=R/2	65.32	101.3	124.0	552.2	1.459	39.4	0.254	0.04	512
r=R	114.18	164.1	387.5	284.7	1.016	12.5	0.081	0.08	1377

C. Neutral Model

The 2.5-D neutral atom sub-model is based on techniques that have been successfully used to calculate thermal transport view factors [51]. This technique is possible due to the large mean free path for neutral atoms and provides order of magnitude savings in run-time compared to a simple 2.5-D steady-state Monte Carlo simulation that was used in preliminary versions of the code. As described in references [refThesis] and [refJPC03], the "view factor" formulation uses the Boundary Mesh to determine the neutral atom distribution and temperature regardless of the Internal Mesh type or resolution. The Neutral Atom Sub-Model accommodates axisymmetric propellant feed configurations, including hollow cathode and plenum configurations used in conventional thrusters. Local temperatures are assigned to each feed location and

atoms emitted from these locations are assumed at the thermal velocity determined by that temperature. Atoms that collide with the thruster walls are spectrally reemitted at the predefined local temperature of the incident wall. This functionality is desirable for conventional ion thrusters where the neutral propellant temperatures at the cathode and plenum feeds can differ by almost an order of magnitude and large variations in wall temperature exist [52]. The local wall temperatures are determined from thermal models [52] or experimental measurements [refJPC05].

For the first iteration of DCM, a uniform volume-averaged ionization rate is assumed in the Neutral Atom Sub-Model to expedite solution convergence. During subsequent iterations, the Neutral Atom Sub-Model uses the species density distributions determined in the Primary and Ion Diffusion sub-models. The Internal Mesh and Boundary Mesh are used to track the neutral atom temperatures and densities that are passed to other sub-models. The grid transparency to neutral atoms, ζ_o , is determined from the product of the geometric open area fraction and is adjusted by the Clausing factor to account for the thickness of the grids [55]. The sum of neutral losses at the "Ion Optics" elements of the Boundary Mesh gives the propellant efficiency per the Neutral Atom Sub-Model by Equation 4.1-1. Further details of the Neutral Atom Sub-Model theory and formulation are given in Reference [refThesis].

The main sources of neutrals in this sub-model are the propellant feeds; however, neutrals are also "re-created" when ions recombine with electrons. Ion recombination predominantly occurs on chamber surfaces and results in an effective neutral flux from the interior chamber surfaces. The Ion Diffusion Sub-Model determines the flux of ions to the chamber surfaces, where incident ions are assumed to undergo three-body recombination and are then spectrally reemitted as neutrals with the mean Maxwellian velocity per the local temperature of the incident wall. In this way, all the wall elements are treated as "sources" of neutrals. The flux of ions to the chamber walls is calculated by the Ion Diffusion Sub-Model and is treated as a source of neutrals in the global neutral atom continuity matrix [refJPC03].

D. Electron Collision Sub-Model

DC ring-cusp ion thruster plasmas are populated by high-energy "primary" electrons that are emitted from the cathode and lower-energy "secondary" electrons. The following section describes the methods used to account for the collisions of these electrons with other species of the plasma, including each other. In the Electron Collision Sub-Model, the ionization rates due to both electron species are found and summed to yield the total ionization rate

$$\dot{n}_i = \dot{n}_i^p + \dot{n}_i^s \qquad [4.3\text{-}1]$$

Other results from this sub-model, such as secondary electron production rates and the rate of loss of primary electron energy to the secondary population, are used in the Electron Thermal Sub-Model. Charge-exchange (CEX) ionization does not affect the total number of ions inside the chamber so it is not considered in this sub-model; however, the CEX effects on ion motion are considered in the Ion Diffusion Sub-Model. In general, the primaries are treated using a particle tracking algorithm, while the secondaries are considered to be a thermalized component of the quasi-neutral plasma.

Primary electrons ("primaries") represent the fundamental input of energy to the discharge chamber. The degree of utilization of this energy for creating a uniform density of beam ions is directly related to the overall efficiency of the thruster. Thus, it is important to be able to identify the general behavior, distribution, and interactions of primaries in the discharge chamber. The mean free path for a primary in an ion thruster discharge chamber is large enough that a particle-tracking method, with collisions to describe interactions with other species, is sufficient to describe their behavior. The Boris-type algorithm used to track the primary electrons and the methods for treating the various collisions with other plasma species is discussed in detail in references [refJPC04] and [refThesis]. An example of the path of a *single* primary electron particle in the NSTAR discharge chamber is shown in Figure 4.3-2. As expected, the particle originates at the hollow cathode orifice and is magnetically confined at the cusps, reflected from cathode potential surfaces, scattered by elastic collisions, and lost to an anode surface.

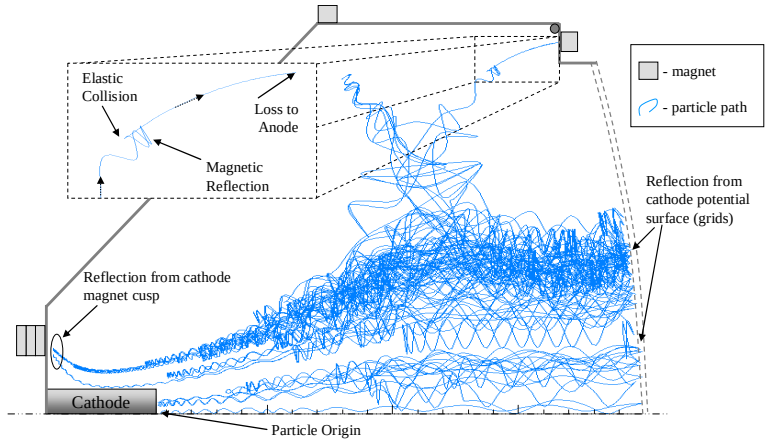

Figure 4.3-2. Simulated Path of a Single Primary Electron Inside the NSTAR Discharge Chamber

Secondary Electron Energy Distribution and Ionization

In general, the secondaries are assumed to have a Maxwellian velocity distribution; however, results from similar plasma discharges suggest that high-energy electrons in the tail of the Maxwellian distribution can become depleted, resulting in a "depleted tail" distribution [60]. Since the degree to which this occurs in ion thrusters is unknown at this time, the Electron Collision Sub-Model approximates the depleted tail distribution with a corrected temperature for inelastic collisions. To simulate this tail depletion a secondary inelastic collision fraction, f_{inel}, is chosen. The product of this fraction and the secondary electron temperature, T_s (note: T_s is determined by the Electron Thermal Sub-Model), yields the secondary electron temperature for inelastic collisions, T_s^{inel}, such that

$$T_s^{inel} = f_{inel} T_s \qquad [4.3\text{-}20]$$

Inelastic collisions for secondaries, such as those that contribute to electron cross-field diffusion, are still assumed to behave at the secondary electron temperature, T_s. The secondary inelastic collision fraction may also be used to approximate an augmented tail distribution. With this approximation, the ionization due to secondary electrons is added to the total volumetric ionization rate for each cell using

$$\dot{n}_i^s = K_{iz}^s n_o\, n_s + K_{iz}^{+s} n_i\, n_s \qquad [4.3\text{-}21]$$

where the temperature, T_s^{inel}, is used to find the rate constant. Since primaries are assumed to join the secondary population immediately following inelastic collisions, the production rate of secondary electrons due to both primary collisions and secondary electron ionization is

$$\dot{n}_s = 2\dot{n}_i^p + \dot{n}_{ex}^p + \dot{n}_{slow}^p + \dot{n}_i^s \qquad [4.3\text{-}22]$$

which is used to determine T_s in the Electron Thermal Sub-Model.

An example of the path of a *single* primary electron particle in the NSTAR discharge chamber is shown in Figure 4.3-2. As expected, the particle originates at the hollow cathode orifice and is magnetically confined at the cusps, reflected from cathode potential surfaces, scattered by elastic collisions, and lost to an anode surface.

F. Ion Optics Model

The CEX2D ion optics model developed at JPL determines extraction grids transparency to ions, $\zeta_i(n_i)$, and neutrals, ζ_o. The results of the ion optics model are also used to predict grid life and examine grid performance9. Once a steady-state solution is reached by the overall discharge model, the radially-dependent conditions just upstream of the grids can be used in a 3-D optic code that gives detailed projection of grid wear and life10.

G. Ion Diffusion Sub-Model

The Ion Diffusion Sub-Model uses the ion generation rates found in the Electron Collision Sub-Model to determine the ion density distribution on the Internal Mesh. To describe ion diffusion, a classical ambipolar ion diffusion equation is derived from the combined single ion and electron motion equations. This equation is then recast to include a correction for non-classical perpendicular diffusion as a function of the relative importance of electron-ion collisions. These equations are formulated to determine the *total* ion densities and fluxes in the thruster. With this solution, the double ion densities are approximated using double-to-single ion generation rates and a simple time-stepping algorithm. The single and double ion densities are then used to determine the beam current and the loss rate of ions to the chamber walls.

Ion Diffusion Theory

The motion of the ions in an ion thruster-type discharge can be described by separately considering their behavior parallel and perpendicular to the magnetic field. The parallel motion is described using a classical ambipolar treatment; however, for computational models of similar plasma regimes, the perpendicular motion is described using either classical or non-classical descriptions, or some combination [49,33]. In this formulation, the classical ambipolar diffusion equation is derived for partially ionized plasma of single ions, unequal ion and electron generation rates, and non-uniform temperatures.

Anisotropic Mobility from Coupled Ion and Electron Motion

The motion of plasma electrons and ions are coupled by their mutual Coulomb interactions and are often treated using ambipolar diffusion as discussed in references [50,66,61]. For magnetized plasma, these treatments assume a regime of equal generation rates of electrons and ions where divergences of the species fluxes may be equated. For a DC discharge this is not necessarily the case since the generation of secondary electrons from collisions of high-energy primary electrons causes an imbalance of the generation rates of secondary electrons and ions. Another characteristic of DC discharges that is commonly ignored is the effect of electron temperature gradients that may be non-negligible in some regions of the chamber. An ambipolar plasma equation is developed below to describe the coupled electron and ion motion for a DC discharge with non-uniform ion and secondary production rates and temperatures.

The ambipolar mobility equations are determined by combining the ion and secondary electron momentum equations. Assuming quasi-neutral plasma of singly charged ions the momentum equations are

$$\mathbf{R}_i + \mathbf{u}_i m_i \dot{n}_i = ne\mathbf{E} + ne\mathbf{u}_i \times \mathbf{B} - k\nabla\left(nT_i\right) \qquad [4.5\text{-}11]$$

$$\mathbf{R}_e + \mathbf{u}_e m_e \dot{n}_e = -ne\mathbf{E} - ne\mathbf{u}_e \times \mathbf{B} - k\nabla\left(nT_e\right) \qquad [4.5\text{-}12]$$

where $q = e$ for ions and $q = -e$ for electrons. $\mathbf{R}_i$ and $\mathbf{R}_e$ are the ion and electron momentum transfer due to collisions and are given in the appendix. Considering motion only parallel and perpendicular to the B-field (|| and ⊥, respectively) and utilizing anisotropic mobility tensors, the momentum equations may be combined to describe the coupled ion-electron motion with the expression

$$\dot{n}_i = -\nabla \cdot \left(\underline{\underline{\mathbf{M}}}_i \nabla\left(nT_i\right) + \underline{\underline{\mathbf{M}}}_e \nabla\left(nT_e\right) + M_E^{\perp} n E^{\perp} \right) \qquad [4.5\text{-}31]$$

where

$$\underline{\underline{\mathbf{M}}}_i \equiv \begin{bmatrix} M_i & 0 \\ 0 & M_i^{\perp} \end{bmatrix} \;,\; \underline{\underline{\mathbf{M}}}_e \equiv \begin{bmatrix} M_e & 0 \\ 0 & M_e^{\perp} \end{bmatrix} \;,\; M_E^{\perp} = \frac{\mu_i \mu_e^{\perp} - \mu_e \mu_i^{\perp}}{\mu_e + \mu_i}$$

$$M_i = \frac{\mu_e \mu_{ii} + \mu_i \mu_{ei}}{\mu_e + \mu_i} \;,\; M_e = \frac{\mu_e \mu_{ie} + \mu_i \mu_{ee}}{\mu_e + \mu_i} \;,\; M_i^{\perp} = \frac{\mu_e \mu_{ii}^{\perp} + \mu_i \mu_{ei}^{\perp}}{\mu_e + \mu_i} \;,\; M_e^{\perp} = \frac{\mu_e \mu_{ie}^{\perp} + \mu_i \mu_{ee}^{\perp}}{\mu_e + \mu_i} \qquad [4.5\text{-}32]$$

The mobilities, μ, used in this equation are defined in the Appendix. The specifics of the derivation of Equation 4.5-31 are given in Reference [refThesis].

With approximations of the species temperatures, perpendicular electric field, ion production rates, and species collision frequencies, the ion motion equation, Equation 4.5-31, may be used to approximate the

plasma density distribution and ion fluxes of weakly ionized plasma. As discussed in references [66,61], the perpendicular electric field can be nearly "short-circuited" in discharges where large imbalances of fluxes along the magnetic field lines are possible. This is commonly the case for ring-cusp ion thruster discharges [67]. This "short-circuit effect" was identified by Simon [68] for finite length plasma columns in conducting containers, and is also described in Reference [69]. Therefore, to first order, the effects of the perpendicular electric fields in the bulk of the plasma are assumed negligible such that $E^{\perp} \approx 0$, simplifying the ion motion equation to

$$\dot{n}_i = -\nabla \cdot \left(\underline{\underline{\mathbf{M}}}_i \nabla \left(nT_i \right) + \underline{\underline{\mathbf{M}}}_e \nabla \left(nT_e \right) \right) \qquad [4.5\text{-}33]$$

Non-Classical Mobility

To this point the perpendicular motion has been assumed to obey classical diffusion for partially ionized plasma, where the electron-neutral collisions are assumed important [50]. To aid the discussion below, two new collision terms are defined. The frequency $\nu_{e\text{-}n}$ represents all the collisions in the neutral reference frame. For this problem the effective electron-neutral-centered collision frequency, $\nu_{e\text{-}o}$, is defined by

$$\nu_{e-o} \equiv \nu_{eo} + \nu_{e-gen} \qquad [4.5\text{-}34]$$

where the effective collision frequency for electron generation, $\nu_{e\text{-}gen}$, is considered to be neutral centered since the drift velocity of the electrons produced from collisions is assumed equal to the neutral drift velocity. The second frequency defined here is $\nu_{e\text{-}i}$, which represents all electron collisions in the ion reference frame. For this problem the effective electron-ion-centered collision frequency, $\nu_{e\text{-}i}$, is identically equal to the electron-ion collision frequency since no other ion-centered collisions are assumed:

$$\nu_{e-i} \equiv \nu_{ei} \qquad [4.5\text{-}35]$$

These parameters, $\nu_{e\text{-}i}$ and $\nu_{e\text{-}n}$, are used below for a mixture technique to determine the appropriate coefficient for perpendicular electron diffusion. In this technique it is assumed that higher $\nu_{e\text{-}i}$, in comparison to $\nu_{e\text{-}o}$, is indicative of more fully ionized plasma. Early results from DCM showed that in the on-axis regions of the discharge plasma the effective electron-ion collision frequency, $\nu_{e\text{-}i}$, is on order of the effective electron-neutral collisions, $\nu_{e\text{-}o}$. In these "intermediately ionized" regions, it is reasonable to consider that the perpendicular electron diffusion is somewhere between that of weakly and fully ionized plasma. Schweitzer and Mitchner [70] proposed mixture rules between weakly ionized (Lorentzian) and fully ionized plasma approximations to estimate the tensor conductivity for the entire range of plasma ionization levels; however this method is prohibitively complex. The following discussion presents a simple mixture technique to describe electron perpendicular transport for plasma regions that are between weakly and fully ionized plasma.

The classical description for perpendicular transport of electrons that is given above is sufficient for weakly ionized regions [50]; however, in fully ionized regions, i.e. as $\nu_{e\text{-}i}/\nu_{e\text{-}o} \rightarrow \infty$, a different method is typically used. A classical derivation of motion in fully ionized plasma yields a B^{-2} dependence for the perpendicular diffusion that is not observed in most experiments [50,49]. Bohm [71] introduced a relationship that describes the perpendicular diffusion of fully ionized plasma as inversely proportional to the magnetic field by

$$D_{\perp} = D_B \equiv \frac{kT_e}{16eB} \qquad [4.5\text{-}36]$$

where $\Gamma_{\perp} = D_{\perp} \nabla_{\perp} n$. The Bohm diffusion coefficient, D_B, has shown agreement with several experiments of fully ionized plasmas [50]. For stable discharges, Bohm diffusion has shown to provide sufficient damping to prevent the exponential growth of azimuthal drift instabilities [71,49,69].

Computational models of Hall thruster plasma, which are in a similar regime as ion thrusters, have demonstrated good agreement with experiments by uniformly adding a fraction of Bohm diffusion to the weakly ionized approximation for perpendicular electron mobility [49]. Arakawa's model (described in Section 2.4) suggests that Bohm diffusion may also be important for ion thrusters [33]. To assess the non-uniform importance of Bohm-type non-classical diffusion for the Ion Diffusion Sub-Model, Equation 4.5-

37 was developed to weigh the classical and non-classical perpendicular mobility of the electrons per the relative dominance of the electron-neutral-centered or electron-ion-centered collisions

$$\left(M_e^{\perp}\right)_{eff} = \frac{\nu_{e-o}}{\nu_{e-o} + \gamma_{nc}\nu_{e-i}} M_e^{\perp} + \frac{\gamma_{nc}\nu_{e-i}}{\nu_{e-o} + \gamma_{nc}\nu_{e-i}} M_B^{\perp} \qquad [4.5\text{-}37]$$

where "Bohm mobility" is defined by

$$M_B^{\perp} \equiv \frac{k}{16eB} \qquad [4.5\text{-}38]$$

The non-classical diffusion parameter, γ_{nc}, serves to mitigate the influence of the Bohm mobility in partially-ionized regions. This parameter was found to best match experimental results using $\gamma_{nc} \approx 1/4$. For non-zero values of γ_{nc}, the effective perpendicular electron mobility, $\left(M_e^{\perp}\right)_{eff}$, yields fully classical mobility for very weakly ionized regions, and Bohm mobility for fully ionized plasmas. Using Equation 4.5-37 the effective anisotropic mobility for electrons is

$$\left(\underline{\underline{\mathbf{M}}}_e\right)_{eff} \equiv \begin{bmatrix} M_e & 0 \\ 0 & \left(M_e^{\perp}\right)_{eff} \end{bmatrix} \qquad [4.5\text{-}39]$$

The final ion motion equation is then

$$\dot{n}_i = -\nabla \cdot \left(\underline{\underline{\mathbf{M}}}_i \nabla\left(nT_i\right) + \left(\underline{\underline{\mathbf{M}}}_e\right)_{eff} \nabla\left(nT_e\right) \right) \qquad [4.5\text{-}40]$$

Formulation of Equation 4.5-40 in a control volume analysis for the orthogonal Internal Mesh and the ion flux boundary conditions are discussed in Reference [refThesis]. Since ion energy is not conserved in this model, a method for estimating the ion temperature is derived from experimental results that show the ion temperature is generally between the neutral temperature and the electron temperature for ion thruster-type plasma conditions [63]. These experimental results suggest that the ion temperature is about one-half to one order of magnitude less than the electron temperature depending on ion mass. For the results presented in here, the local ion temperature of the relatively massive xenon (used for the thruster simulations herein) is assumed to be one-tenth the local electron temperature, $T_i \sim 0.1T_e$.

Double Ion Correction

NSTAR beam measurements have shown double-to-single ion current ratios on the order of 0.15 [16]. A method to correct the single ion solution for the effects of double ions is given below. The double ion density near the grids is calculated and used to determine a corrected beam current to compare with experimental results.

The local generation rates of double ions are determined by comparing the relative rates of total and double ion production using the rate constants discussed in Section 4.3 and Appendix G. The Ion Optics Sub-Model assumes that double ions follow the same path lines as the single ions solution [12]. In this way, the double ion density, n_{++}, is determined from the local double ion production rates by the continuity equation for double ions:

$$\frac{\partial n_{++}}{\partial t} + \nabla \cdot \left(n_{++} u_+ \sqrt{2} \right) = \dot{n}_{++} \qquad [4.5\text{-}50]$$

where the double ion drift velocities, due to their charge, are assumed to be greater than the single ion drift velocities, u_+, by a factor of $\sqrt{2}$. This equation is applied at the end of an iteration using the upwind time-step control volume formulation described in Appendix G. The effect of the double ions on the beam current density is determined using the ratio of double ions to total ions

$$R_{++} = n_{++} / n_i \qquad [4.5\text{-}51]$$

where only single and double ions are assumed. Assuming ions enter the ion optics sheath with Bohm velocity, for an element on the Boundary Mesh with transparency to ions, ζ_i, the single ion beam current density becomes

$$j_B^+ = \zeta_i e u_+^{Bohm} n_+ = \zeta_i e u_+^{Bohm} n_i \left(1 - R_{++}\right) \qquad [4.5\text{-}52]$$

where n_+ and u_+^{Bohm} are the density and Bohm velocity for single ions. The double ion beam current density for the same element will then be

$$j_B^{++} = \zeta_i 2e\left(\sqrt{2}u_+^{Bohm}\right)n_{++} = \sqrt{8}\zeta_i e u_+^{Bohm} n_i R_{++} \qquad [4.5\text{-}53]$$

As discussed in Section 2, the discharge propellant efficiency is the ratio of propellant that leaves the thruster as an ion (of any charge) to the flow rate of propellant into the chamber. By this definition, the actual propellant efficiency is calculated by summing over the ion flux contributions from all Boundary elements, *m*, such that

$$\eta_{ud} = \frac{\sum\left[j_B^+ + j_B^{++}/2\right]_m A_m}{e\dot{m}_d} = \frac{\left(J_B^+ + J_B^{++}/2\right)m_i}{e\dot{m}_d} \qquad [4.5\text{-}54]$$

To compare with experimental data, the Ion Diffusion Sub-Model also calculates discharge propellant efficiency that would be observed in experiments where the efficiency is not corrected for double ion content

$$\eta_{ud[*]} = \frac{\sum\left[j_B^+ + j_B^{++}\right]_m A_m}{e\dot{m}_d} = \frac{\left(J_B^+ + J_B^{++}\right)m_i}{e\dot{m}_d} \qquad [4.5\text{-}55]$$

Since the double ion correction results in a slight increase in the rate of total ions to the beam, the ion flux to the internal surfaces is normalized to maintain ion continuity.

Ion Diffusion Post-Run Analysis

For post-run analysis, the ratio of the electron-neutral-centered and electron-ion-centered collision frequencies from equations 4.5-34 and 4.5-35 is used to assess the effective level of ionization of the plasma. This "electron collision ratio" is defined as

$$\delta_\nu \equiv \nu_{e-o}/\nu_{e-i} \qquad [4.5\text{-}59]$$

In a similar manner, the ratio of the diffusion coefficients from Equation 4.5-42 are used to quantify the "magnetization," δ_D, of the plasma motion in different regions of the thruster by

$$\delta_D = D_{\|}/D_{\perp} \qquad [4.5\text{-}60]$$

H. Electron Thermal Model

The following section describes a method for approximating the secondary electron temperature. This is done by first using effective potentials to obtain the electron flux and then imposing electron energy conservation to find T_s. Combining the electron continuity and momentum equation give a simplified electron equation [50]

$$\dot{n}_s = \nabla \cdot \left(\underbrace{-\underline{\underline{\mu}}_s^* n\mathbf{E} - \underline{\underline{\mu}}_s^* \nabla\left(nT_s\right)}_{\Gamma_s} \right) \qquad [4.6\text{-}3]$$

where

$$\underline{\underline{\mu}}_s^* \equiv \frac{e}{m_e(\nu_{e-i} + \nu_{e-o})}\begin{bmatrix} 1 & 0 \\ 0 & \frac{1}{1+\Omega_e^2} \end{bmatrix} \qquad [4.6\text{-}4]$$

and Ω_e is the electron Hall term. Using this formulation and assuming the electron temperatures are approximately constant across a given surface of a computational volume, the gradients in the electron flux is expressed using an *effective* potential, ψ, by

$$\Gamma_s = -\underline{\underline{\mu}}_s^* n \nabla \psi \qquad [4.6\text{-}7]$$

where

$$\psi \equiv T_s \ln \frac{n}{n_c} - \phi \qquad [4.6\text{-}8]$$

Equation 4.6-3 is rewritten simply in terms of the effective potential, plasma density, and electron generation rate as

$$\dot{n}_s = -\nabla \cdot \underline{\underline{\mu_s^*}} n \nabla \psi \qquad [4.6\text{-}9]$$

At the discharge chamber boundaries the secondary electrons are assumed repelled from cathode potential surfaces, such as the cathode keeper and ion extraction grids, while the electrons are assumed almost entirely lost at the magnetic cusp and that electron flux between the cusps approximately equals the ion flux [67]. The electron flux, Equation 4.6-7, derived from the solution for effective potential, Equation 4.6-9, is used in the electron energy equation below to find secondary electron temperature. Assuming inelastic collisions are the dominate energy source/sink term for steady-state ion thruster conditions, the electron energy equation may be defined as [refThesis]

$$\nabla \cdot \left(\frac{5}{2} kT\Gamma_s + \mathbf{q} \right) = -Q_s + Q_p \qquad [4.6\text{-}27]$$

where $-Q_s$ is the change in energy density from inelastic secondary electron collisions with heavy species and Q_p is the change energy density from primary electron collisions

Ignoring thermoelectric effects, the electron heat flux vector, **q**, is defined by anisotropic thermal conductivity $\mathbf{q} = -\underline{\underline{\kappa}} \nabla T_s$, where $\underline{\underline{\kappa}}$ is the thermal conductivity in a magnetic field determined by Braginskii [72]. This equation, with the above boundary conditions, is used to approximate the secondary electron temperature.

IV. Results

In this section, results from DCM are compared with experimental data from the NSTAR thruster. For the chosen operating conditions, the model gives good agreement with NSTAR beam profiles and performance curves. The model analyses show that the peak observed in the NSTAR beam profile is due to double ions that are created by over-confinement of primary electrons on the thruster axis. This over-confinement of primaries on-axis also results in neutral density just inside the grids that is over an order of magnitude less on-axis than that at the radial extent of the grids. DCM was used to perform a first-level design analysis of the NSTAR thruster that showed that the performance and beam flatness may be increased significantly by simply increasing the middle magnet ring strength.

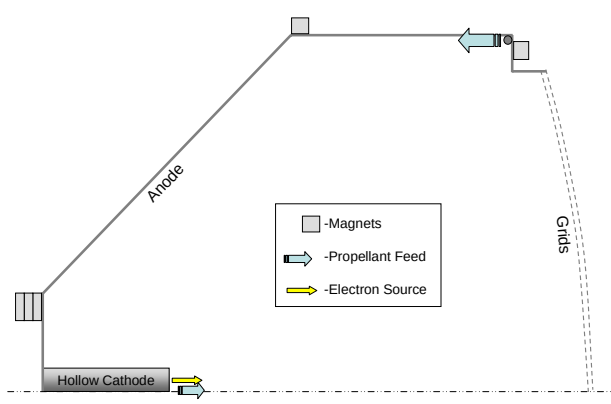

Figure 5.1-1. NSTAR Thruster Geometry

A. Inputs and Assumptions

A 2-D diagram of the NSTAR thruster geometry used for the model is shown in Figure 5.1-1. Most of the propellant comes from the plenum located next to the grid magnet ring, while the rest (~10-20%) of the propellant enters through the hollow cathode. The magnetic field is created by rings of rectangular samarium cobalt (SmCo) magnets. The cathode magnets are significantly larger than the middle and grid magnets and are stacked three-deep to create a strong magnetic field in the

cathode region. The grid and middle rings are very similar in size. The exact sizes and locations of the magnets were used in the Magnetostatic Sub-Model. Comparisons of the measured magnetic field and that predicted by the model are given in Appendix F and show very good agreement in the experimentally measured regions. A contour plot of the magnetic field for the default NSTAR configuration and a modified configuration are shown in Figure 5.3-3.

The TH15 and TH12 beginning-of-life throttle points for NSTAR are shown in Table 5.1-1. The grid voltages, along with the grid geometry, were used to find the ion and neutral transparency in the Ion Optics Sub-Model. The current of primaries from the hollow cathode is determined from charge conservation by $J_p = J_D - J_{screen}$, where J_{screen} is the ion current to the screen grid determined by the Ion Diffusion Sub-Model.

Table 5.1-1. NSTAR Throttle Points [Beginning of Life]

Throttle Points	Main Flow [sccm]	Cathode Flow [sccm]	J_B [A]	J_D [A]	V_D [V]	V_B [V]	V_{accel} [V]	Model Specific Inputs	
								Vp [V]	Tp [eV]
TH12	19.85	2.92	1.59	10.87	25.4	1100	-249	21	3
TH15	23.42	3.73	1.76	13.13	25.1	1100	-249	20	2.5

In the absence of a near-cathode model, the two thruster inputs to DCM that are not determined directly from thruster operating conditions are the accelerated half-Maxwellian characteristics of the primary electrons (V_p and T_p). As described in Appendix G, for hollow cathode discharges such as NSTAR, initial estimates of these parameters are inferred from the discharge voltage, and measurements of cathode operating voltage, plasma potential, and cathode insert electron temperature. Experimental measurements [73] show the electron temperature of a NSTAR-type hollow cathode plasma is on the order of 2-3eV; therefore, T_p ~ 2-3eV was used. The primary electron accelerating voltage, V_p, is related to the discharge voltage but cannot be determined exactly without knowing the accelerating potential structure in the near-cathode region. As presented in Appendix G, this voltage can be estimated using measurements of the NSTAR cathode operating voltage (V_c ~6V) and plasma potential (ϕ ~2-3V) [73] as $V_p \sim V_D + \phi - V_c$. These estimates of V_p and T_p were used as starting point values, and were then adjusted to attain the desired beam current for a given throttle point. For the results herein, the values of V_p and T_p that were used to compare with NSTAR data are shown in Table 5.1-1.

The Electron Collision Sub-Model assumes that the secondary inelastic collision factor, f_{inel}, is uniform throughout the discharge. Preliminary results from the model were used to determine a value that provided reasonable agreement with the secondary electron measurements from [65]. Depending on the assumed primary electron energy, values ranging from 0.7 to 0.9 showed good agreement with the experimental measurements. To minimize the number of free parameters, the average value of f_{inel} = 0.8 was assumed for all DCM results discussed herein.

cc

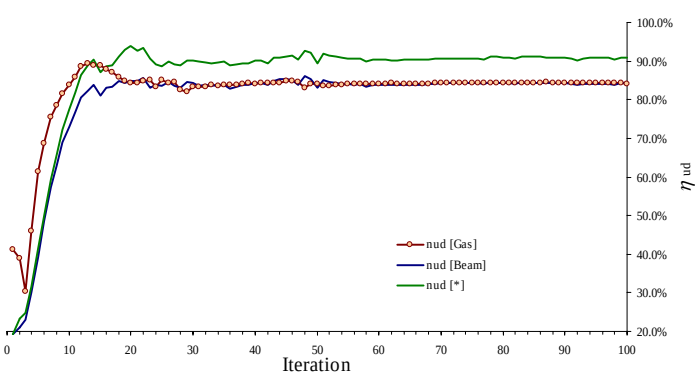

against experimental data for both
ı losses to the wall were very large, resulting in unreasonably poor performance. For γ_{nc} = 0 (weakly ionized assumption) the ion and double ion densities were very high on-axis, yielding unreasonably low beam flatness values. Good agreement with TH15 experimental data was generally found for γ_{nc} ~ ¼, therefore this value was used for all simulations.

Figure 5.2-1. Propellant Efficiency vs. Iteration for TH15

B. Model Results and Experimental Comparison

The results in this section are for DCM at the TH15 operating point from Table 5.1-1, unless otherwise noted. Model results at TH12 are given in Appendix H. To avoid large gradients in the early iterations, DCM assumes a low primary electron current (~5-10%) for the first iteration and then incrementally increases the primary current to its full value, after which the model converges to a steady state solution.

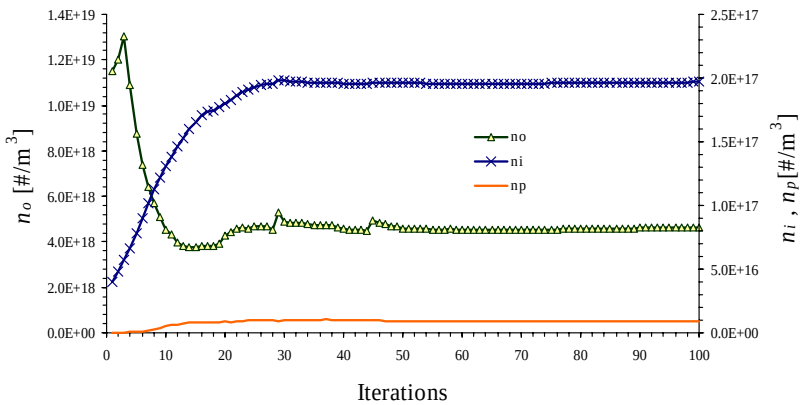

Figure 5.2-2. Volume-Averaged Densities vs. Iteration for TH15

Solution Convergence

Figure 5.2-1 shows the results for propellant efficiency vs. iteration where the primary current reached full strength after 10 iterations. In this figure nud[Gas], nud[Beam], and nud[*] are the propellant efficiencies per equations 4.1-1, 4.1-2, and 4.1-3, respectively.

At the end of an iteration, the volume-averaged densities are determined. The convergence of these averaged density values, shown in Figure 5.2-2, is indicative of the convergence of the non-uniform values on the Internal Mesh. Contour plots of parameters on the Internal Mesh are given below.

Comparison with Experimental Results

The beam current density profiles along the dished exit plane of the thruster, as calculated by DCM, are shown in Figure 5.2-3. In this figure, jB[+] assumes that all beam ions are singly charged (i.e., jB[+] = $\left[j_B^+ + j_B^{++}/2 \right]$), while jB[++] includes doubly charged ion effects (i.e., jB[++] = $j_B^+ + j_B^{++}$). The variables j_B^+ and j_B^{++} are described in equations 4.5-52 and 4.5-53. Comparing these profiles shows the radially dependent effect of double ions on measured beam current. For this case, the model agrees with experimental data that show that the peak on the axis of the beam profile is largely due to double ion current. The "Data" profile is extrapolated from the NSTAR TH15 data found in Reference [7]. The jB[++] profile shows generally good agreement with the Data profile, though some discrepancy is found near r ~ 3cm and r ~ 13cm. Figure 5.2-3 also includes the neutral atom density predicted by the model just inside the grids, showing over an order of magnitude drop in neutral density from the edge of the grids to the center.

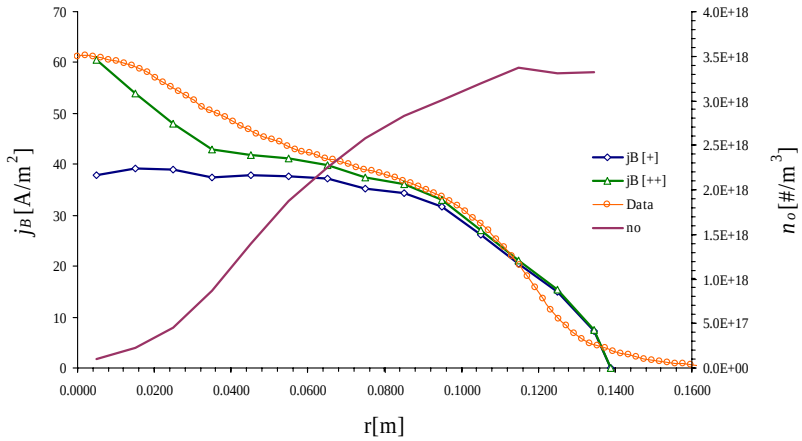

Figure 5.2-3. Beam and Neutral Density Profiles at Grids for TH15

The 8,200 hour test [7] also included a performance sensitivity analysis that was conducted after the thruster had operated for several thousand hours. During this analysis, the main flow rate was changed over a range of ± 9%, while the beam current was kept constant, resulting in the discharge performance trend shown in Figure 5.2-4. For each value of main flow rate used in the analysis, the beam current, 1.76A, was kept constant by adjusting the discharge voltage and current. To compare the performance sensitivity of the model with this data, DCM was first used to match the performance at the nominal (TH15) operating condition at the middle of the curve. Then, holding all other parameters constant, the flow rate and discharge current in the model were changed to the maximum and minimum values used in the tests. The resulting discharge performance curve in Figure 5.2-4 suggests that DCM yields good agreement over the range of performance shown. In this analysis, the primary electron energy was held constant. This approximation was made since cathode flow rate was held constant in the experimental analysis and the cathode operating conditions have been shown to be strongly dependent on this parameter [73]. For the assumptions of this comparison, the model over-predicts the propellant efficiency by 1.5-2%. This discrepancy may be related to lack of knowledge of the near-cathode conditions for the different operating conditions.

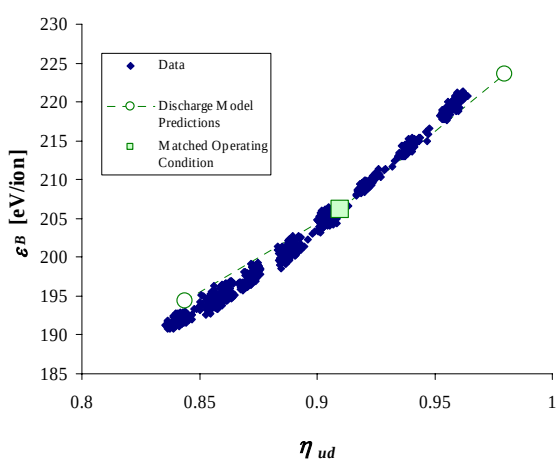

Figure 5.2-4. Comparison of DCM and NSTAR Performance Curve Data at TH15

Discharge Performance Parameters

Table 5.2-1 shows several of the discharge parameters (defined below) that were determined by DCM at TH15. These parameters are important to understanding the fundamental behavior of the discharge, as described in Reference [32]. Where possible, these values are compared with the NSTAR data from Reference [7]. The values for $\eta_{ud\,[*]}$ and ε_B are very similar since they are determined by the conditions that define the throttle points from Table 5.1-1. The parameters in Table 5.2-1 are defined as follows:

$\eta_{ud\,[*]}$ – discharge propellant efficiency defined in Equation 4.1-3

η_{ud} – discharge propellant efficiency defined in Equation 4.1-2

ε_B – discharge loss [eV/ion]

J_{B++} /J_{B+} - ratio of beam current due to doubly- and singly charged ions

J_i – current of ions created in discharge [A]

J_{ip} – current of ions created in discharge by primaries [A]

n_i – average density of ions [m^{-3}]

n_p – average density of primary electrons [m^{-3}]

n_o – average density of neutrals [m^{-3}]

f_A – fraction of ion current to anode surfaces

f_B – fraction of ion current to the beam

f_C – fraction of ion current to cathode surfaces

F_B – beam flatness as defined by jB [++] profile

F_{B*} – beam flatness as defined by jB [+] profile

The results in Table 5.2-1 show that DCM predicts double ion content within the range observed by experimental measurements [16]. Previous measurements have shown that efficient ion thruster discharges should extract ~50% of the ions to the beams [32]; however, DCM predicts f_B = 29% for NSTAR TH15. This result is improved slightly in the modified NSTAR design in Section 5.3.

Table 5.2-1. Discharge Performance Parameters

(NSTAR - TH15 Simulation vs. Data)

Discharge Parameters	$\eta_{ud\,[*]}$	η_{ud}	ε_B	J_{B++}/J_{B+}	J_i	J_{ip}	n_i	n_p	n_o	f_A	f_B	f_C	F_B	F_{B*}
Units	%	%	eV/ion	-	A	A	m-3	m-3	m-3	-	-	-	-	-
Model Results	90.9	85.6	187	0.129	6.08	3.73	$1.97 *10^{17}$	$9.25 *10^{15}$	$4.64 *10^{18}$	0.66	0.29	0.05	0.47	0.674
Data	90.8	83.8-85.7	187	0.126-0.184									0.47	

Electron Power Loss

The Electron Collision and Electron Thermal sub-models track the power lost by the primary and secondary electron populations. Table 5.2-2 shows the percentage of the total input power lost by all the electron power loss mechanisms considered by the model. The *total* input energy is defined by the total primary current and the average primary energy. The secondary electron energy losses are referenced to the *total* input power to assess their contribution to the overall power balance of the discharge. Therefore, by the following definitions, $P_{ps} = P_{sw} + P_{siz} + P_{sx}$.

P_{ps} – primary power transferred to secondary population

P_{pw} – primary loss to wall

P_{piz} – primary ionization of propellant

P_{px} – primary excitation of propellant

P_{sw} – secondary loss to walls

P_{siz} – secondary ionization of propellant

P_{sx} – secondary excitation of propellant

The results in Table 5.2-2 show that most of the primary energy is transferred to the secondary electrons, and most of the secondary energy is subsequently lost to the chamber walls. These results also show that the primaries contribute to most of the ionization for NSTAR TH15; however, secondaries account for nearly 40% of the ionization. In reference [refJPC05], the results from Table 5.2-2 are compared with results from Micro-Ion thruster simulations to contrast the behavior of conventional and miniature discharges.

Table 5.2-2. Electron Power Loss Mechanisms

(NSTAR TH15)

Mechanism	**Primary Electron Losses**				**Secondary Electron Losses**		
	P_{ps}	P_{pw}	P_{piz}	P_{px}	P_{sw}	P_{siz}	P_{sx}
% of Total Input Power Lost	69%	0.7%	13.7%	16.6%	49.1%	7.5%	12.5%

Two-Dimensional Plots of Discharge Characteristics

DCM generates 2-D data of the non-uniform characteristics of the discharge plasma on the Internal Mesh. In this section, DCM results at the NSTAR TH15 operating condition are presented. The total ion density distribution and some approximate ion streamlines are plotted on the Internal Mesh in Figure 5.2-5. This plot shows that the ions are preferentially lost at the cusps and the grids; however, some loss between the cusps occurs. The contours of double- to single-ion density ratio, Figure 5.2-6, show that the double ions reside primarily on-axis. This phenomenon can be explained by the high density of high-energy primary electrons on-axis as shown in Figure 5.2-7 and the slightly higher secondary electron temperature in that region, Figure 5.2-8. These combined effects also result in a high ionization rate on axis, Figure 5.2-9. The values from figures 5.2-6–5.2-8, and the rate constants derived from Appendix G, show that the double ionization on-axis is almost entirely (>99%) due to primary electron collisions.

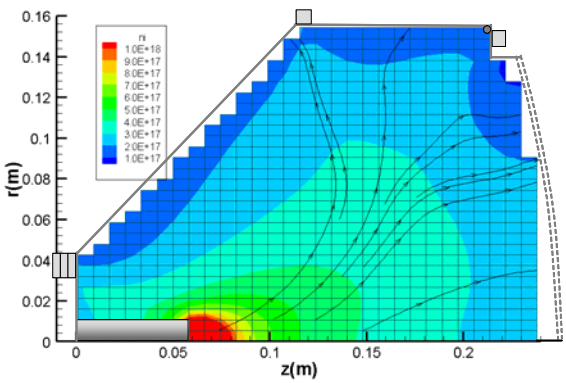

Figure 5.2-5. Total Ion Density [m^{-3}] and Streamlines - TH15

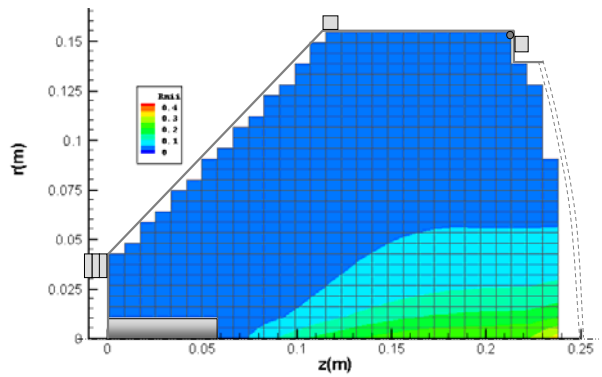

Figure 5.2-6. Double Ion Ratio (R++ = n++/ni) - TH15

The neutral density predicted by the model, Figure 5.2-10, is highly non-uniform. From the neutral and ion density plots it is apparent that the plasma is nearly 50% ionized in the on-axis region near the grids. In the presence of high-energy electrons, this region experiences a relatively high ratio of double- to single-ion generation rates.

DCM predicts the non-classical behavior of the plasma by considering the relative frequency of electron-neutral-centered and electron-ion-centered collisions. Figure 5.2-11 presents a plot of the distribution of the ratio of these frequencies, $\delta_\nu = \nu_{e\text{-}n}/\nu_{e\text{-}i}$, which shows that intermediate levels of ionization exists throughout the chamber and increasingly on-axis. This shows that the non-classical correction to the diffusion is important to the perpendicular diffusion results. The resulting level of anisotropy of the plasma motion, predicted by the model, is measured by the ratio of parallel and perpendicular diffusion coefficients, $\delta_D = D_\parallel / D_\perp$. The distribution of δ_D predicted by DCM is plotted in Figure 5.2-12. This plot suggests that the plasma is nearly unmagnetized in the highly ionized regions on-axis, and of course, in the low magnetic field region in the middle of the thruster.

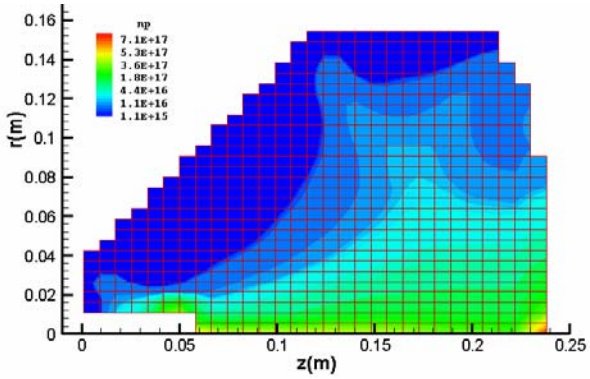

Figure 5.2-7. Primary Electron Density [m^{-3}] - TH15

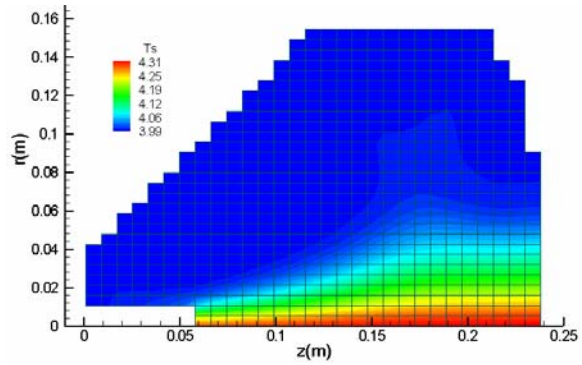

Figure 5.2-8. Secondary Electron Temperature [eV] - TH15

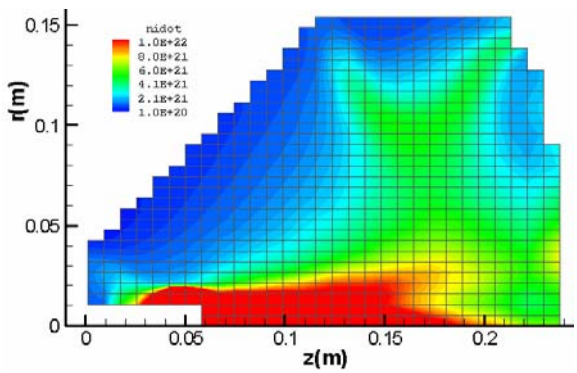

Figure 5.2-9. Ion Generation Rate Density [s^{-1} m^{-3}] - TH15

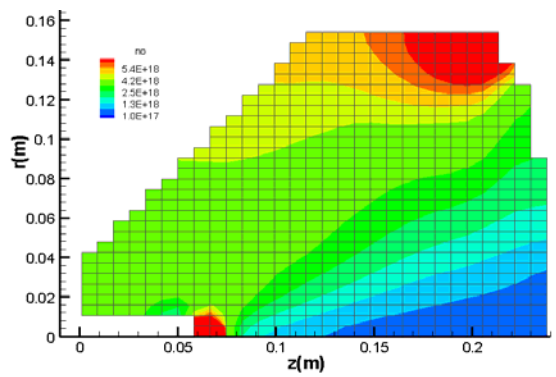

Figure 5.2-10. Neutral Atom Density [m^{-3}] - TH15

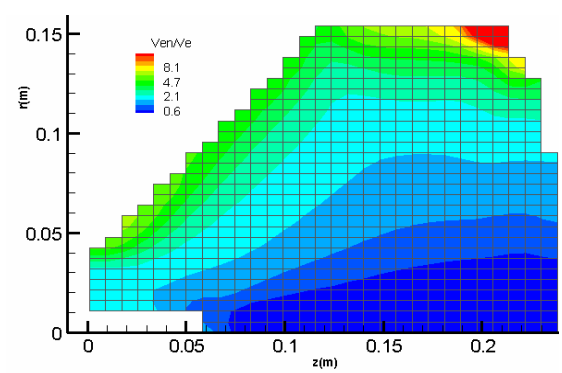

Figure 5.2-11. Electron Collision Frequency Ratio ($\delta_\nu = \nu_{e\text{-}n} / \nu_{e\text{-}i}$) - TH15

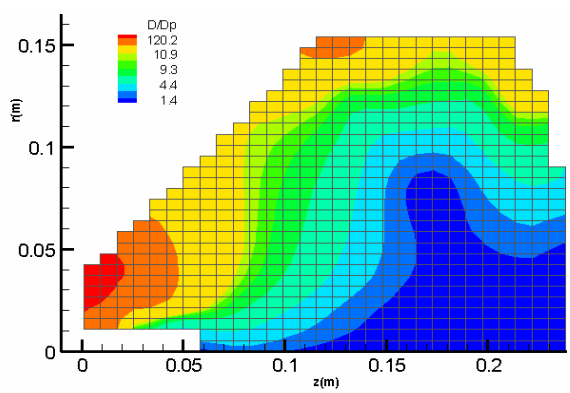

Figure 5.2-12. Ion Diffusion Coefficient Ratio ($\delta_D = D_{||}/D_{\perp}$) - TH15

C. NSTAR Design Analysis

DCM was used to perform a design analysis for the NSTAR thruster by doubling the strength of the magnets on the middle magnetic ring. The middle magnet ring was strengthened by increasing the length (along the axis of magnetization) for the permanent magnet dimension that is used by the magnetostatic solution (refer to Figure 5.3-3). The modified thruster design was simulated at TH15 operating conditions. The impact of this modification on the discharge parameters is shown in Table 5.3-1 by comparing discharge performance with the original NSTAR configuration.

Table 5.3-1. Discharge Performance Parameters

(NSTAR TH15 - Original vs. Modified Design)

Discharge Parameters	η_{ud} [*]	η_{ud}	ε_B	J_{B++}/J_{B+}	J_i	J_{ip}	n_i	n_p	n_o	f_A	f_B	f_C	F_B	F_{B*}
Units	%	%	eV/ion	-	A	A	m-3	m-3	m-3	-	-	-	-	-
Original	90.9	84.5	187	0.16	6.08	3.73	$1.97 *10^{17}$	$9.25 *10^{15}$	$4.64 *10^{18}$	0.66	0.29	0.05	0.47	0.674
Modified	94.2	90.2	179	0.093	5.94	3.83	$1.85 *10^{17}$	$7.99 *10^{15}$	$3.96 *10^{18}$	0.64	0.31	0.05	0.68	0.71

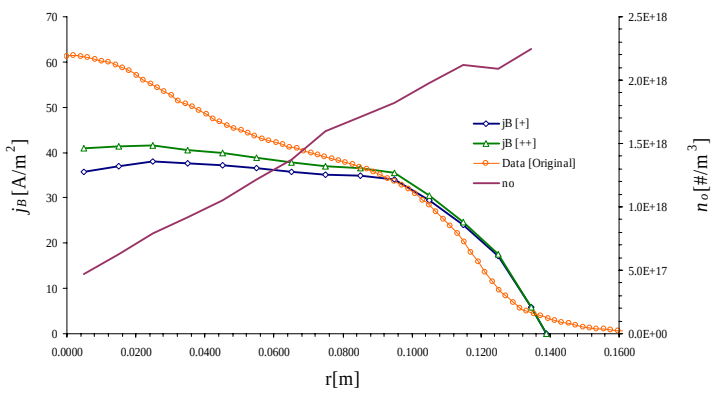

Figure 5.3-1. Beam and Neutral Density Profiles for Dimply Modified NSTAR Thruster - TH15
(note: "Data" values are from original thruster configuration)

Figure 5.3-1 shows the beam and neutral density profiles that were predicted by DCM for the modified NSTAR design. The experimental TH15 beam profile "Data" for the original NSTAR design is included in this figure for reference. According to these results, a simple modification to the existing NSTAR design can yield increased performance and will likely result in longer life due to increased beam flatness, greater neutral atom uniformity across the grids, and lower double ion content. These results should be verified by experimental testing but this type of simple analysis shows that DCM can serve as a useful tool for aiding in the optimization of thruster life and performance.

Table 5.3-2. Electron Power Loss Mechanisms

(NSTAR TH15- Original vs. Modified Design)

Mechanism / Thruster	**Primary Electron Losses**				**Secondary Electron Losses**		
	P_{ps}	P_{pw}	P_{piz}	P_{px}	P_{sw}	P_{siz}	P_{sx}
Original	69.0%	0.7%	13.7%	16.6%	49.1%	7.5%	12.5%
Modified	65.7%	4.2%	13.7%	16.4%	48.3%	6.6%	10.9%

Figure 5.3-2 shows the primary electron distribution for the modified NSTAR thruster. Comparing this result to those for the original thruster, Figure 5.2-7, suggests that the more uniform profile of the modified thruster is due in large part to the more even distribution of primary electrons. The tendency for the primary electrons to not be mainly confined to the thruster axis, as in the original design, can be understood by comparing the magnetic field lines in Figure 5.3-3. For the modified thruster, a large percentage of the near-axis magnetic field lines will guide the primaries away from the axis, instead of confining them to the

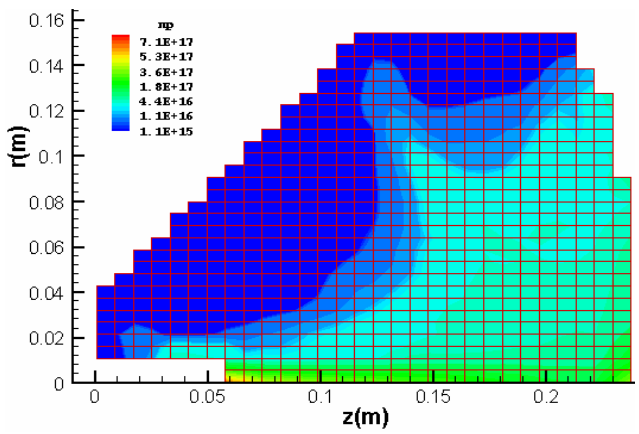

Figure 5.3-2. Modified NSTAR – Primary Electron Density [m^{-3}] - TH15

axis as the original design appears to do. In this way, the modified design improves primary electron utilization.

Comparing the electron power loss mechanisms, Table 5.3-2, would actually lead a designer to believe that the modified design would result in lower performance due to the higher loss to the walls, and lower power due to ionization. The discrepancy arises from the power wasted by the original design in double ionization near the axis and the greater propensity of the modified design to extract single ions to the beam.

The original and modified NSTAR magnetic fields are shown in Figure 5.3-3. Comparing the contours of these two plots shows that the original NSTAR field closes the 27 Gauss contour between the mid and cathode magnet rings, while the modified design closes the 37 Gauss contour at this location. Between the mid and grid rings the original NSTAR closes the 30 Gauss contour and the modified design closes the 46 Gauss contour. This correlation of improved performance with closing the higher B-field contour (near ~40 Gauss) agrees with previous studies [17,18] that experimentally observed this phenomenon for ring-cusp ion thrusters.

V. Conclusions

DCM represents a significant advancement in the state of the art of ion thruster discharge modeling because it does not rely on the results of simple analytical models to assess performance. Results from DCM agree well with several ion thruster operating conditions at conventional and miniature ion thruster sizes. The information provided by the model on the non-uniform discharge parameters, (i.e., densities, production rates, etc.) allows for detailed analysis of the discharge performance for a given configuration. The results show that the primary electrons cause at least 60% of the ionization and that their behavior is very important to thruster performance for all thruster sizes.

Results from the NSTAR thruster show that the double ion peak measured in experimental beam profiles is due to the magnetic field, which confines the primary electrons to the near-axis region. This confinement results in high ion density and low neutral density on-axis, which, when coupled with a high concentration of energetic primaries, results in high levels of double ionization. This illustrates the importance of considering non-uniform neutral and primary densities. Comparing these results with a modified NSTAR design shows that a higher ion extraction fraction, f_B, is achieved by guiding the primary electrons to regions where they are most likely to make single ions that will be extracted to the beam. On the other hand, simply increasing primary confinement does not guarantee better performance.

Proper treatment of secondary electron motion is necessary to accurately predict the plasma diffusion. DCM results for both thruster sizes show that the perpendicular diffusion of secondary electrons is described by combining classical treatment with Bohm diffusion. The effect of non-classical perpendicular electron mobility showed good agreement with experimental data for values of γ_{nc} near ¼. The specific mechanisms related to this value for γ_{nc} have not been identified; however, in the context of the treatment herein, a value of γ_{nc} between 0 and 1 suggests that ion thruster plasma may be considered intermediately ionized, as described in Section 4.5. Good agreement with experimental measurements of T_s were found by assuming some tail depletion of the secondary population, namely $f_{inel} \sim 0.8$.

In addition to aiding thruster design, the detailed information from DCM provides useful input for wear models of the discharge cathode and ion extraction grids. By working with wear models, DCM can be used to assess long-term thruster performance and validate thruster life. These results may in turn be used to improve the thruster design to maximize the thruster lifetime performance.

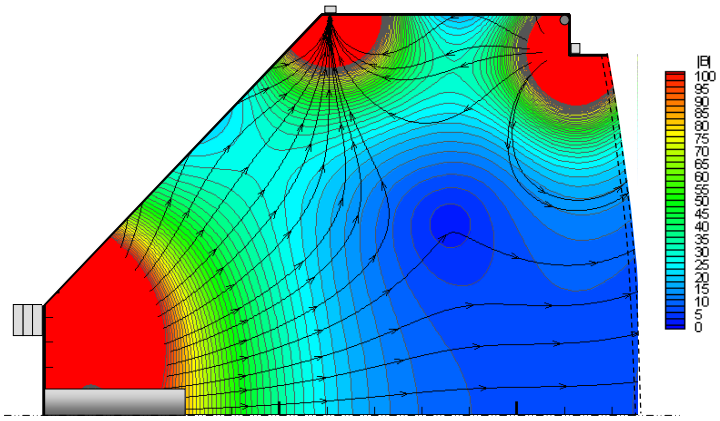

Figure 5.3-3a. Original NSTAR Magnetic Field [Gauss] with Example Magnetic Field Lines

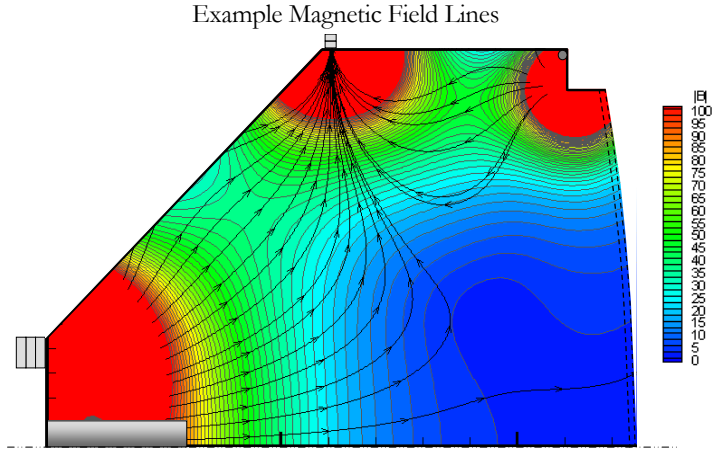

Figure 5.3-3b. Modified NSTAR Magnetic Field [Gauss] with Example Magnetic Field Lines (note: double mid magnetic ring)

VI. Future Work

In future analyses, DCM can be used to iterate through a large design space to allow optimization of the performance of the miniature thruster. The large surface-to-volume ratio yields inherently large discharge losses; however, significant improvements to the discharge efficiency are possible through optimization of the primary confinement within the limits of discharge stability. Future experimental efforts for the miniature discharge should focus on fully characterizing the discharge instabilities that occur at high field strengths and identifying these stability limits. Optimization of magnet strength, magnet configuration, and cathode placement should be performed once the final cathode technology is chosen. Improvements to miniature cathode technologies for the small thruster are imperative to the viability of the thruster and should be investigated further.

In future versions of DCM detailed modeling of the near-cathode region will provide accurate information of the primary electron energy distribution [8]. Knowledge of the near-cathode electron energies will provide self-consistent values for the two DCM input parameters that are not simply identified by operational thruster inputs: V_p and T_p, the primary half-Maxwellian characteristics. Combining DCM with cathode and grid wear models will allow for long-term performance assessments and thruster life predictions [9,12].

DCM currently uses Bohm diffusion to approximate non-classical effects. Experimental measurements within the discharge chamber should be used to determine the existence and importance of anomalous effects such as azimuthal drift waves and ion acoustic waves, which may arise from the high-velocity stream of electrons emitted from the cathode. Knowledge of the importance of these types of non-classical mechanisms will improve the accuracy of DCM.

DCM can also be improved with a better treatment of the secondary electron population. For example, a more detailed electron energy balance treatment for primaries and secondaries will improve the predictions of secondary electron temperature and the secondary inelastic collision parameter. Another way to improve the secondary electron treatment is to use a magnetically aligned mesh ("B-Mesh"), which was used in original versions of the model [47,48]. This complex meshing technique was abandoned in this study for reasons discussed in Section 4.1; however, it is much better suited to treating the highly anisotropic nature of the electron motion, and should be considered for future versions of the model. The simpler formulation of the electron motion equation that is possible with the B-Mesh may allow the electric fields to be solved self-consistently. In this way, the effects, or lack thereof, of perpendicular electric fields can be assessed. With a reliable electric field solution, DCM may also be expanded to include the effects of discharge instabilities [15]. Future experimental efforts should characterize discharge instabilities for high magnetic field cusp configurations to assure that these effects are accurately reproduced by DCM.

.

Acknowledgments

The research described in this paper was carried out by the Jet Propulsion Laboratory, California Institute of Technology, under a contract with the National Aeronautics and Space Administration in support of Project Prometheus.

References

[1] J. Polk, et al., "An Overview of the Results from an 8200 Hour Wear Test of the NSTAR Ion Thruster," AIAA 99-2446
[2] A. Sengupta, J. Brophy, and K. Goodfellow, "Status of the Extended Life Test of the DS1 Flight Spare Ion Engine after 30,352 Hours of Operation, AIAA-2003-4558, 40th AIAA Joint Propulsion Conference, Fort Lauderdale, FL, July 11-14, 2004
[3] Arakawa Y., Ishihara K., "A Numerical Code for Cusped Ion Thrusters," IEPC-91-118, 1991
[4] Arakawa Y., Yamada T., "Monte Carlo Simulations of Primary Electron Motions in Cusped Discharge Chambers," IEPC paper AIAA-90-2654
[5] Arakawa Y., Wilbur P., "Discharge Plasma Calculations in Cusped Ion Thrusters Using the Finite Element Method," IEPC-88-079, 1988
[6] Brophy J., Wilbur P., "Simple Performance Model for Ring and Line Cusp Ion Thrusters," AIAA Journal, Vol. 23, pp. 1731-1736, 1985
[7] J. Polk, et al., "An Overview of the Nuclear Electric Xenon Ion System (NEXIS) Program", AIAA-2003-4713, 40th AIAA Joint Propulsion Conference, Fort Lauderdale, FL, July 11-14, 2004
[8] R. Wirz, et al., "Miniature Ion Engine for Precision Formation Flying," AIAA-2004-4115, 40th Joint Propulsion Conference, Ft. Lauderdale, FL, July 11-14, 2004
[9] Brophy J.R. Katz I., Polk J., Anderson J., "Numerical Simulations of Ion Thruster Accelerator Grid Erosion," AIAA-2002-4261, 38th AIAA/ASME/SAE/ASEE Joint Propulsion Conference & Exhibit, Indianapolis, IN, July 2002
[10] J. Andersen, J., Katz, I., "Numerical Simulation of Two- Grid Ion Optics Using a 3D Code," AIAA-2004-3782, 40th Joint Propulsion Conference, Ft. Lauderdale, FL, July 11-14, 2004
[11] I. Mikellides, I. Katz, D. Goebel and J. Polk, "Theoretical Model of Hollow Cathode Insert Plasma," AIAA-2004-3817, 40th Joint Propulsion Conference, Ft. Lauderdale, FL, July 11-14, 2004
[12] Ira Katz, I. Mikellides, D. Goebel, "Model of the Plasma Potential Distribution in the Plume of a Hollow Cathode," AIAA-2004-4108, 40th Joint Propulsion Conference, Ft. Lauderdale, FL, July 11-14, 2004
[13] Wirz R., Katz I., 'A Preliminary 2-D Computational Model of an Ion Thruster Discharge Chamber', AIAA-2003-5163, 39th AIAA/ASME/SAE/ASEE Joint Propulsion Conference, Huntsville, AL, July 20-23, 2003
[14] M. Mitchner and C. Kruger, Partially Ionized Gases, John Wiley & Sons, New York, pp. 88-93, 1973.
[15] Nickel, J., Imre, K., Register, D., Trajmar, S., "Total Electron Scattering Cross Sections: I. He, Ne, Ar, Xe," J. Phys. B: At. Mol. Phys. 18 (1985) 125-133
[16] D. Goebel, K. Jameson, R. Watkins, I. Katz "Cathode and Keeper Plasma Measurements Using an Ultra-Fast Miniature Scanning Probe," AIAA-2004-3430, 40th Joint Propulsion Conference, Ft. Lauderdale, FL, July 11-14, 2004
[17] A. Sengupta, D. Goebel, G. Tynan, R. Doerner, S. Snyder, "Experimentally Determined Neutral Density and Plasma Parameters in a 30 CM Ion Engine," AIAA-2004-3613, 40th Joint Propulsion Conference, Ft. Lauderdale, FL, July 11-14, 2004
[18] L. Spitzer, Jr., Physics of Fully Ionized Gases, Interscience, New York, p. 127-135, 1962.
[19] D. Rapp and P. Englander-Golden, "Total Cross-Sections for Ionization and Attachment in Gases by Electron Impact, I. Positive Ionization," J. Chem. Phys., V. 43, pp. 1464-1479 1965
[20] L.T. Specht, et. al., "Electron Ionization and Excitation Coefficients for Argon, Krypton and Xenon in the Low E/N Region," JAP, V. 51, pp. 166-170, Jan. 1980.
[21] Krall, N., Liewer, Phy. Rev. A 4, 2094 (1971)
[22] J. P. Boris, Relativistic plasma simulations—Optimization of a hybrid code, in, Proc. 4th Conf on Num Sim of Plasmas, NRL Washington, Washington DC, 1970
[23] Chen F., "Plasma Physics and Controlled Fusion Vol. 1," 2nd Edition, ©1984
[24] Goldston, R., Rutherford, P., " Introduction to Plasma Physics," 1995
[25] Lieberman, M., Lichtenberg, A., "Principles of Plasma Discharges and Materials Processing," ©1994
[26] J. Miller, et al., "Xenon Charge Exchange Cross Sections for Electrostatic Thruster Models," Journal of Applied Physics, Vol 91,No 3, Feb 2002
[27] Katz, I., Anderson, J., Polk, J., and Brophy, J., "Plasma Generation Near an Ion Engine Discharge Chamber Hollow Cathode," AIAA-2003-5161, to be presented at the 2003 Joint Propulsion Conference, Huntsville, AL, July 20-23, 2003
[28] Leung, K., Hershkowitz, N., MacKenzie, R., "Plasma Confinement by Localized Cusps," Physics of Fluids, Vol. 19, No. 7, July 1976
[refJPC05] R. Wirz, AIAA Paper 2005-3887, 41st AIAA/ASME/SAE/ASEE Joint Propulsion Conference, Tucson, AZ, 2005.

Appendix

Collisions Terms

The neutral drift velocities are typically assumed negligible compared to the electron and ion drift velocities for ion thrusters, thus $\mathbf{R}_i$ and $\mathbf{R}_e$ may be written as

$$\mathbf{R}_i \equiv nm_i \sum_a \langle \nu_{ia} \rangle (\mathbf{u}_i - \mathbf{u}_a) = nm_i \nu_{ie} (\mathbf{u}_i - \mathbf{u}_e) + nm_i \nu_{io} \mathbf{u}_i + nm_i \nu_{CEX} \mathbf{u}_i \qquad [4.5\text{-}15]$$

$$\mathbf{R}_e \equiv nm_e \sum_a \langle \nu_{ea} \rangle (\mathbf{u}_e - \mathbf{u}_a) = nm_e \nu_{ei} (\mathbf{u}_e - \mathbf{u}_i) + nm_e \nu_{eo} \mathbf{u}_e \qquad [4.5\text{-}16]$$

To combine equations 4.5-11 and 4.5-12, the generation and momentum transfer terms on the LHS are recast. The generation terms are expressed using effective collision frequencies as follows:

$$\nu_{i-gen} = \dot{n}_i / n \quad ; \quad \nu_{e-gen} = \dot{n}_e / n \qquad [4.5\text{-}13]$$

The momentum transfer terms are then rewritten in terms of collision frequencies as well. In typical ion thruster discharges, the electron-ion and ion-electron Coulomb collision frequencies, ν_{ei} and ν_{ie}, cannot be ignored in comparison to the electron-neutral, ν_{eo}, and ion-neutral, ν_{io}, collision frequencies. In addition to these collisions, the ion-neutral charge-exchange frequency, ν_{CEX}, is included. The neutral drift velocities are typically assumed negligible compared to the electron and ion drift velocities for ion thrusters…
Combining these expressions, the momentum equations become…
where the neutral-centered ion and electron collision frequencies are…

$$\nu_{i-o} \equiv \nu_{io} + \nu_{CEX} + \nu_{i-gen} \quad ; \quad \nu_{e-o} \equiv \nu_{eo} + \nu_{e-gen} \qquad [4.5\text{-}20]$$

Collision frequencies ν_{ei}, ν_{io}, ν_{CEX}, and ν_{eo} are defined in Appendix G. The electron temperatures used for Equation 4.5-19 are determined by the Electron Thermal Sub-Model.